Ultrahigh Specific Strength by Bayesian Optimization of Carbon Nanolattices

Peter Serles,* Jinwook Yeo, Michel Haché, Pedro Guerra Demingos, Jonathan Kong, Pascal Kiefer, Somayajulu Dhulipala, Boran Kumral, Katherine Jia, Shuo Yang, Tianjie Feng, Charles Jia, Pulickel M. Ajayan, Carlos M. Portela, Martin Wegener, Jane Howe, Chandra Veer Singh, Yu Zou, Seunghwa Ryu,* and Tobin Filleter*

Nanoarchitected materials are at the frontier of metamaterial design and have set the benchmark for mechanical performance in several contemporary applications. However, traditional nanoarchitected designs with conventional topologies exhibit poor stress distributions and induce premature nodal failure. Here, using multi-objective Bayesian optimization and two-photon polymerization, optimized carbon nanolattices with an exceptional specific strength of 2.03 MPa m³ kg⁻¹ at low densities <215 kg m⁻³ are created. Generative design optimization provides experimental improvements in strength and Young's modulus by as much as 118% and 68%, respectively, at equivalent densities with entirely different lattice failure responses. Additionally, the reduction of nanolattice strut diameters to 300 nm produces a unique high-strength carbon with a pyrolysis-induced atomic gradient of 94% sp² aromatic carbon and low oxygen impurities. Using multi-focus multi-photon polymerization, a millimeter-scalable metamaterial consisting of 18.75 million lattice cells with nanometer dimensions is demonstrated. Combining Bayesian optimized designs and nanoarchitected pyrolyzed carbon, the optimal nanostructures exhibit the strength of carbon steel at the density of Styrofoam offering unparalleled capabilities in light-weighting, fuel reduction, and contemporary design applications.

1. Introduction

Nanoarchitected materials have set the benchmark for non-monolithic mechanical performance including the highest recorded specific strength,[1,2] specific stiffness,[3,4] and energy absorption characteristics.[5,6] These exceptional properties are achieved by the combination of three synergistic properties – structurally efficient geometries for the loading conditions,[7,8] high-performance constituent materials,[9,10] and nanoscale size effects[11,12] – which come together to produce some of the highest performing materials ever created. As such, these metamaterials hold promise to revolutionize materials design in light-weighting for aerospace,[1] ballistics absorption for defense,[5] ultrafast response for optics,[13] and many other contemporary design applications. Nonetheless, despite rapid progress and significant promise, the ultrahigh specific strength and specific stiffness

P. Serles, B. Kumral, K. Jia, S. Yang, T. Filleter
Department of Mechanical & Industrial Engineering
University of Toronto
5 King's College Road, Toronto M5S 3G8, Canada
E-mail: PSerles@mie.utoronto.ca; filleter@mie.utoronto.ca

J. Yeo, S. Ryu
Department of Mechanical Engineering
Korea Advanced Institute of Science and Technology (KAIST)
291 Daehak-ro, Daejeon, Yuseong-gu 34141, Republic of Korea
E-mail: ryush@kaist.ac.kr

The ORCID identification number(s) for the author(s) of this article can be found under https://doi.org/10.1002/adma.202410651

M. Haché, P. G. Demingos, J. Kong, J. Howe, C. V. Singh, Y. Zou
Department of Materials Science and Engineering
University of Toronto
184 College St, Toronto M5S 3E4, Canada

P. Kiefer, M. Wegener
Institute of Applied Physics
Karlsruhe Institute of Technology
Kaiserstraße 12, 76131 Karlsruhe, Germany

S. Dhulipala, C. M. Portela
Department of Mechanical Engineering
Massachusetts Institute of Technology
77 Massachusetts Ave., Cambridge 02139, USA

T. Feng, C. Jia
Department of Chemical Engineering & Applied Chemistry
University of Toronto
200 College St, Toronto M5S 3E5, Canada

of nanoarchitected materials remain limited by their geometric performance.[8,14] Over the past decade, an extensive exploration of several dozen nanoarchitected geometries has been conducted including lattices, triply periodic minimal surfaces, gyroids, honeycombs, and hybrid geometries (Figure S1 and Table S1, Supporting Information). However, these investigations have predominantly employed uniform topologies and beam elements which are known to exhibit stress concentrations and fail at the nodes and junctions.[15,16] Several geometries have accounted for this including plate-lattice hybrids[1] and shell triply periodic minimal surfaces,[3] but these rely on high relative densities or closed-cell topologies with poor scalability and higher manufacturing complexity. In parallel, nanoarchitecture performance has been further limited by the constituent material performance. Pyrolytic carbon offers a specific strength of nearly 10 GPa cm^3 g^{-1}, which approaches that of diamond when the strut diameters are confined to nanoscale thicknesses,[11,12] but the atomic mechanism driving this nanoscale confinement effect remains unresolved thereby limiting its widescale optimization and deployment.[10]

Here, we employ a multi-objective Bayesian optimization (MBO) algorithm for beam element design in combination with high sp^2 bonded nanoscale pyrolytic carbon to produce lightweight carbon nanolattices with ultrahigh-specific strengths and scalability. Finite element analysis (FEA) derived training datasets facilitate predictive generative modeling with three-objective Bayesian optimization by optimizing linear elastic responses to compression and shear while minimizing density. We build upon prior implementations of machine learning algorithms in experimental solid mechanics and design[17–20] with a focus on scalable open-cell topologies and high-quality smaller datasets. This is done using Bayesian optimization, which has been successfully employed to enhance the mechanical properties of macroscopic architected materials,[21–24] alongside nanoscale strengthening to achieve synergistic high mechanical performance. The optimized lattices are produced using two-photon polymerization (2PP) nanoscale additive manufacturing with pyrolysis to produce carbon nanolattices with average strut diameters of 300 and 600 nm. Using localized structural and atomic characterization in parallel with molecular dynamics simulations, we identify increased sp^2 bonding and higher carbon purity in the external shell region of pyrolytic carbon struts with a radial gradient due to pyrolysis, thereby maximizing the specific strength and stiffness of lattices with minimized strut diameters. By concurrently maximizing the mechanical response while minimizing relative density through MBO, in combination with nanoscale strut diameters, these carbon nanolattices achieve the compressive strength of carbon steels (180–360 MPa) with the density of Styrofoam (125–215 kg m^{-3}) which exceeds the specific strengths of equivalent low-density materials by over an order of magnitude.

2. Results

2.1. Generative Modelling for Mechanics

The optimization and validation process of MBO generative modeling is illustrated in **Figure 1a** (detailed algorithm design in Figure S2, Supporting Information). Briefly, the initial lattice structure is broken into its constituent segments for which the four control points are randomly distributed within the design space of the strut length. A continuous profile is formed by the four points using a Bézier curve which is revolved in 3D and each segment is symmetrically applied relative to the nodes. Initial training data is calculated using FEA from randomly generated geometries by evaluating relative density ($\bar{\rho}$), effective Young's modulus ($\bar{E}$), and effective shear modulus ($\bar{\mu}$) for 400 geometries. A 3D hypervolume is then iteratively expanded by maximizing the space enclosed by the normalized values $0<(\bar{E}, \bar{\mu}, \bar{\rho}^{-1})<1$ to identify the Pareto optimum surface until 100 data points are generated via MBO (see Note S1, Supporting Information). From the generative designs that approach the Pareto surface, we select structures that maximize $[\frac{\bar{E}}{\bar{\rho}} \cdot \frac{\bar{\mu}}{\bar{\rho}}]^{0.5}$ thereby designing for the multimodal loading experienced under typical applications. Optimal designs are converted into 3D unit cells that are patterned into 5 × 5 × 5 lattices. Using 2PP nanoscale additive manufacturing, these lattices are produced as an acrylic polymeric structure and subsequently pyrolyzed at 900 °C to convert the crosslinked polymer into a glassy aromatic carbon that is ≈20% of the original size. Finally, the mechanical properties of the nanolattice are determined using nanoscale uniaxial compression to measure Young's modulus (E) and strength (σ).

Four cubic-face centered cubic (CFCC) lattice generative designs with optimized beam shapes are illustrated in Figure 1b which highlights the curved nanolattice beam elements generated by MBO. The MBO lattices frequently show intuitive material redistribution toward the nodes with thinned mid-beam regions to achieve the highest ratio of stiffness to density and eliminate nodal stress concentrations. However, non-intuitive geometries such as the FCC strut of CFCC MBO-1 and the CC strut of CFCC MBO-4 show a taper toward the node yet achieve high optimization valuation suggesting the algorithm may identify optimization methods different from convention. Figure 1c shows field-emission scanning electron microscopy (FESEM) images of a CFCC MBO-3 carbon nanolattice with the strut profile as compared to the model render highlighting the highly conformal geometry despite the complex curvatures and manufacturing complexities. Cross-sectional FESEM images and geometric analysis further show the internal low-density structure and conformal strut geometry (Figures S3 and S4, Supporting Information). The material distribution by MBO is stark in comparison to the standard CFCC carbon nanolattice in Figure 1d with uniform struts. In addition to CFCC generative lattice designs, cubic-body centered cubic (CBCC) lattice MBO generative beam elements were created using the same process to demonstrate the facile translation of this algorithm and manufacturing workflow to a

P. M. Ajayan
Materials Science & Nanoengineering
Rice University
6100 Main St, Houston 77005, USA

M. Wegener
Institute of Nanotechnology
Karlsruhe Institute of Technology
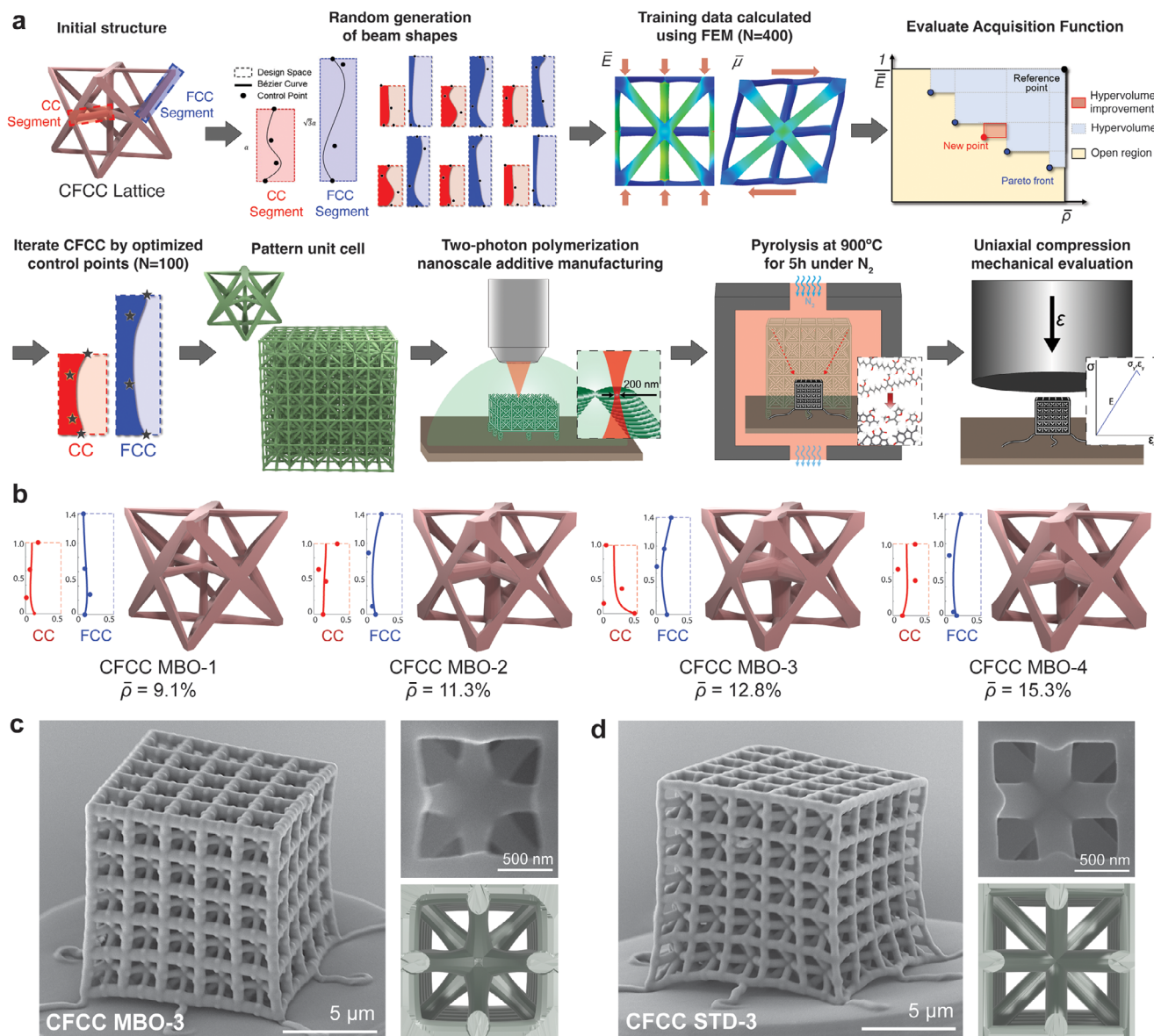Kaiserstraße 12, 76131 Karlsruhe, Germany

**ADVANCED
SCIENCE NEWS**

www.advancedsciencenews.com

**ADVANCED
MATERIALS**

www.advmat.de

Figure 1. Multi-objective Bayesian optimization for generative design of carbon nanolattices with high compressive stiffness and strength at low density. a) Illustration of process workflow. b) The top four MBO CFCC geometries with their 2D Bézier curves. c,d) FESEM images of CFCC MBO-3 and Standard CFCC of equivalent density.

variety of skeleton geometries (Figures S5 and S6, Supporting Information).

The Young's moduli and strength of the four MBO CFCC lattices are presented in **Figure 2a,b** in contrast to standard CFCC lattices of equivalent density to each MBO iteration. We find the MBO-based lattices show increases in Young's modulus by as much as 68% and strength by as much as 118% as compared to a standard geometry with uniform struts. The relative enhancements are statistically significant for all four MBO lattices despite their markedly different cross-sections, indicating no singular dominant beam cross-section for achieving high specific stiffness and strength. Additionally, CBCC lattices with MBO generative elements demonstrate similar mechanical performance en-

hancement highlighting the widescale applicability of this generative technique (Figure S7, Supporting Information). Meanwhile, halving the lattice size and thereby decreasing the strut diameter from 600 to 300 nm shows as much as 75% enhancement in stiffness and 79% enhancement in strength which is in agreement with the trends of carbon nanopillars with equivalent diameters (Figure S8, Supporting Information and Ref. [11]). Further decreasing the strut diameter below 300 nm led to a loss of geometric fidelity in the final part due to voxel print resolution and warping during pyrolysis. Interestingly, while the MBO algorithm seeks to maximize the specific stiffness, the specific strength is greatly enhanced in parallel. As the constituent pyrolytic carbon is linear-elastic prior to fracture failure (Figure S9, Supporting
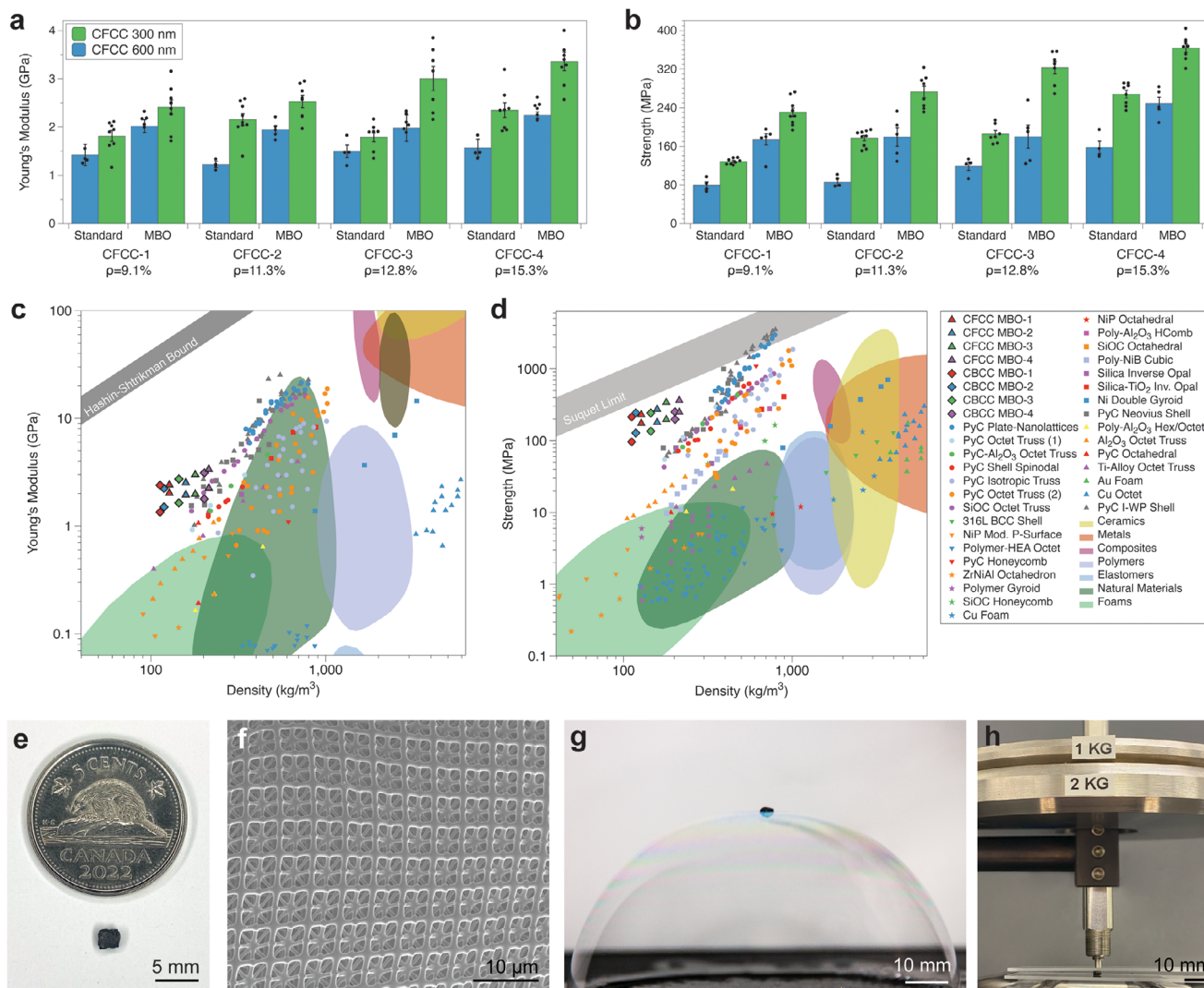
Figure 2. Mechanics and scalability of MBO generative carbon nanolattices. a) Young's moduli and b) the strength of CFCC MBO and standard carbon nanolattices with 600 and 300 nm strut diameters. c,d) Ashby property plots of Young's modulus and strength versus density show CFCC and CBCC nanolattices as compared to prior works and natural materials. The full reference list is in Figure S1 and Table S1 (Supporting Information). Note: Each MBO nanolattice iteration has equivalent densities for both 300 and 600 nm constituent strut diameters, but the 300 nm struts exhibit higher mechanical performance as shown by a vertical shift on the Ashby plot. e) Carbon nanolattice consisting of 18.75 million lattice cells (nickel for scale). f) FESEM image of the nanolattice geometry after pyrolysis. g) Macroscopic nanolattice resting on a bubble, and h) supporting more than one million times its weight, showcasing lightweight and high strength scalability.

Information), improving the stress distribution homogeneity to maximize the stiffness response concurrently leads to maximized strength.

We benchmark the performance of MBO CFCC and CBCC nanolattices to other architected and natural materials using Ashby charts of Young's modulus and strength versus density in Figure 2c,d (benchmark details in Figure S1 and Table S1, Supporting Information). The MBO lattices occupy a distinct regime of high-performance lightweight materials, exhibiting densities comparable to porous foams like Styrofoam ($\rho = 125$–215 kg m^{-3}) but combined with compressive strengths comparable to carbon steels ($\sigma = 180$–360 MPa) and stiffnesses of soft woods ($E = 2.0$–3.5 GPa). The greatest specific strength is achieved by CFCC MBO-3 at 2.03 MPa m^3 kg^{-1} which is more than an or-

der of magnitude higher than other lightweight materials with $\rho = 180$ kg m^{-3} and approaches the Suquet theoretical limit of diamond as noted in Figure 2d.

We also consider the density scaling of the MBO geometries as compared to the standard lattice (Figure S10, Supporting Information). The CFCC and CBCC lattices are stretching-dominated based on Maxwell's criterion which enables mass-efficient structural materials[25–27] and the CFCC standard lattice shows scaling exponents near unity. Yet, the MBO algorithm exhibits reduced scaling exponents for the MBO-1 lattice of $E \propto \bar{\rho}^{0.97}$ and $\sigma \propto \bar{\rho}^{0.93}$ indicating a dominance of stretching elements under load with increased performance at low density. However, despite identical nodal connectivity ratios, the CFCC MBO-3 and Standard lattices exhibit higher scaling exponents. As such, in addition to

2410651 (4 of 11)

**ADVANCED
SCIENCE NEWS**

www.advancedsciencenews.com

**ADVANCED
MATERIALS**

www.advmat.de

nodal connectivity, the beam geometry plays a significant role in loading modality and density scaling which must be taken into account.

Given the detail required to create nanoscale topologies by 2PP, typical nanoarchitected materials are limited to a few hundred μm^3 due to excessive printing times and therefore have yet to demonstrate macroscopic impacts despite their exceptional promise. However, the periodic nature and open-cell topology of CFCC and CBCC nanolattices make them extremely well-suited for multi-focus 2PP.[28] We use a $\lambda = 790$ nm femtosecond Ti:Sa laser with a diffractive optical element and a multilens array to produce 7×7 parallel laser foci,[29] combined with a high-sensitivity photoinitiator for ultrahigh print speeds of $v = 1$ m s^{-1},[30] to increase processing throughput by more than three orders of magnitude compared to our conventional 2PP parameters. Using CFCC MBO-3 for its high performance, we produce $315 \times 315 \times 189 = 18.75$ million lattice cells in under two days totaling $6.3 \times 6.3 \times 3.8$ mm^3 (Figures S11 and S12, Supporting Information). The 18.75 million-cell lattice shows shrinkage during pyrolysis as noted in Figure 2e and we observe high nanolattice fidelity with minor pyrolysis-induced warping as per Figure 2f and Figure S13 (Supporting Information). The relative density after pyrolysis is $\rho = 202$ kg m^{-3} (Figure S14, Supporting Information) which is in close agreement with the ideal $\rho = 179$ kg m^{-3}. Defects are noted to occur along lattice stitching (Figure S15, Supporting Information) but affect fewer than 1% of total lattices. The concurrent lightweight and high-strength characteristics are highlighted in Figure 2g,h as the lattice is light enough to balance upon a bubble but also supports more than one million times its mass. While this does not fully recapitulate the high mechanical performance of the nanolattices, this represents a notable proof step toward the implementation of high-performance carbon nanolattices with macroscopic geometries by high-throughput printing with submicron resolution.

2.2. Nanolattice Optimization

Nanolattices designed by MBO with the probability of hypervolume improvement (PHVI) algorithm offer remarkable structural efficiency which is one of the primary mechanisms contributing to the nanolattice ultrahigh specific strength and stiffness. MBO is the preferred algorithm as it is data-efficient so pairs well with FEA to enable the simultaneous weighting of $\bar{E}$, $\bar{\mu}$, and $\bar{\rho}$. To verify the performance of MBO, we considered other algorithms and acquisition functions commonly used in multi-objective problems and confirmed that MBO most effectively explores the Pareto front, yielding a better distribution of optimal data across the design space (Note S2 and Figures S16 and S17, Supporting Information). The multi-objective optimization plot is presented in **Figure 3a** for the CFCC initial training and MBO data (CBCC plot in Figure S18, Supporting Information). The deviation of the MBO data from the cluster of initial data points indicates a directed optimization approach that favors the low-density regime along the Pareto front. This is due to both higher loading bearing sensitivity of thinner struts to minor deviations in the profile, and the focus on exploration of uncharted design spaces by Bayesian optimization.

Figure 3b shows the distribution of lattice performance with respect to the evaluation metric and Figure 3c shows the evaluation metric performance of the standard, initial data best, and MBO Rank 1 lattice. The CFCC and CBCC lattices were selected as skeleton geometries as they are high-performing lattices in a balance of compressive and shear stiffness.[27] As such, the standard CFCC lattice is well-performing and the best of the randomly generated initial data shows only a 7% improvement (Figure 3c). Conversely, the MBO-1 top-ranked lattice shows a stark increase in the evaluation metric performance by 42% which trends toward the 68% increase in Young's modulus noted experimentally (Figure 2a). Interestingly, nearly all of the initial training data designs and many of the MBO iterations exhibit evaluation metric values below that of the standard lattice. However, MBO, through its dual strategy of exploitation (targeting designs predicted to be optimal) and exploration (seeking designs that clarify the predictive model's uncertainties), facilitates the identification of a diverse range of structures along the Pareto front. The geometries that deviate most from the training data occur during later iterations (Figure S19, Supporting Information) indicating progressive directed optimization throughout the process. As such, despite the lower performance of the initial training data structures, the MBO algorithm nonetheless identifies enhancement mechanisms and generates optimal beam elements with vast improvements. This highlights the MBO algorithm's capability for genuine and targeted generative designs, rather than simply the mimetic output of known geometries.

It should be noted that MBO is based upon the first-order linear elastic response as capturing higher-order mixed-mode failure response in nanoscale pyrolytic carbon requires assumptions about dominant failure modes and excess computational costs. Additionally, the simultaneous evaluation of $\bar{\mu}$ with $\bar{E}$ and $\bar{\rho}$ is included to ensure the material withstands experimental loads that are not perfectly uniaxial. Evaluation which simply considers $\bar{E}$ and $\bar{\rho}$ leads to thick CC struts and zero-thickness of the FCC/BCC struts, thereby only serving perfectly orthogonal loading. Instead, the concurrent evaluation of all three metrics ensures the algorithm does not tend away from the isotropic initial state of the CFCC and CBCC lattices, as evidenced by the Zener ratios of the optimized structures which all have values of within ±0.085 of unity (Figure S20, Supporting Information).

FEA stress distributions highlight the material allocation throughout the strut length which enables this high specific strength and stiffness in Figure 3d,e and Figures S21–S25 (Supporting Information). For the standard lattice, stress fields are discontinuous with highly localized stress concentrations at the ends of vertical members and junctions between diagonal members due to sharp radii and bending stresses. Conversely, the CFCC MBO-3 lattice shows continuous stress fields and tapered reinforcement of vertical members which enables nonlinear stress distributed uniformly throughout the strut length. Interestingly, as noted in Figure 1b, while the MBO lattices frequently show material redistribution which enlarges the nodes to reduce stress concentrations, several designs show non-intuitive design features. This may be due to the combined evaluation of compression and shear, however, these non-intuitive features nonetheless aid in establishing continuous stress fields and effectively translate into high mechanical performance. Figure S23
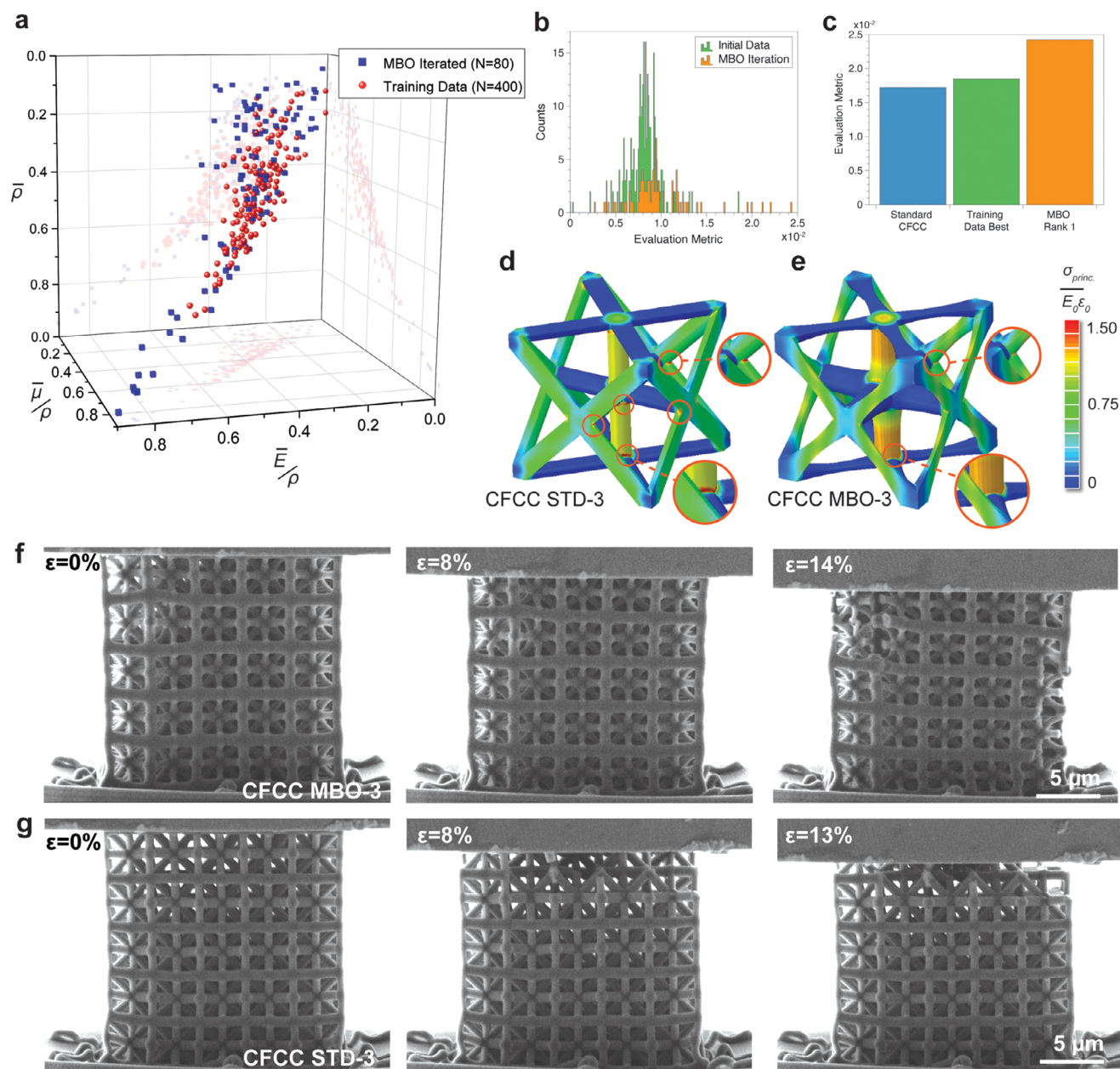
**ADVANCED
SCIENCE NEWS**

www.advancedsciencenews.com

**ADVANCED
MATERIALS**

www.advmat.de

Figure 3. Multi-objective Bayesian optimization mechanisms for mechanical enhancement. a) Multi-objective optimization plot of $\bar{\rho}$, $\bar{E}$, and $\bar{\mu}$ showing the training data and MBO iterated data. b) Density distribution of training and MBO data with respect to the evaluation metric. c) Standard CFCC, Training Data Best, and MBO Rank 1 performance based on the evaluation metric. d,e) FEA Principal Stress distribution plots for CFCC Standard and CFCC MBO-3 geometries of equivalent density. f,g) In situ uniaxial compression of CFCC MBO-3 and CFCC STD-3 lattices, respectively.

(Supporting Information) shows a volumetric plot of stress distribution for CFCC MBO-3 indicating both an elimination of unloaded material and a reduction in high-loading volume. As a result, the entire lattice geometry is recruited to collectively support critical loading thereby enhancing stiffness while the maximum stress is redistributed away from localized nodal regions which increases overall strength and efficiency.

This enhanced stress distribution is demonstrated by in situ uniaxial compression as presented in Figure 3f,g for the CFCC MBO-3 and CFCC STD-3 lattices with 600 nm struts (CFCC

MBO-3 with 300 nm struts in Figure S26 (Supporting Information) and videos in Movies S1 and S2, Supporting Information). The MBO iterated geometry deforms throughout the entire lattice structure under loading in stark contrast to the Standard lattice which exclusively shows deformation of the top layer. At $\epsilon = 8\%$, the MBO lattice shows elastic deformation distributed across all cells while the Standard lattice experiences fracture of the top layer with minimal deformation in the lower lattice. Distributed deformation throughout the MBO lattice indicates homogenized stress transfer by reinforcement of stress
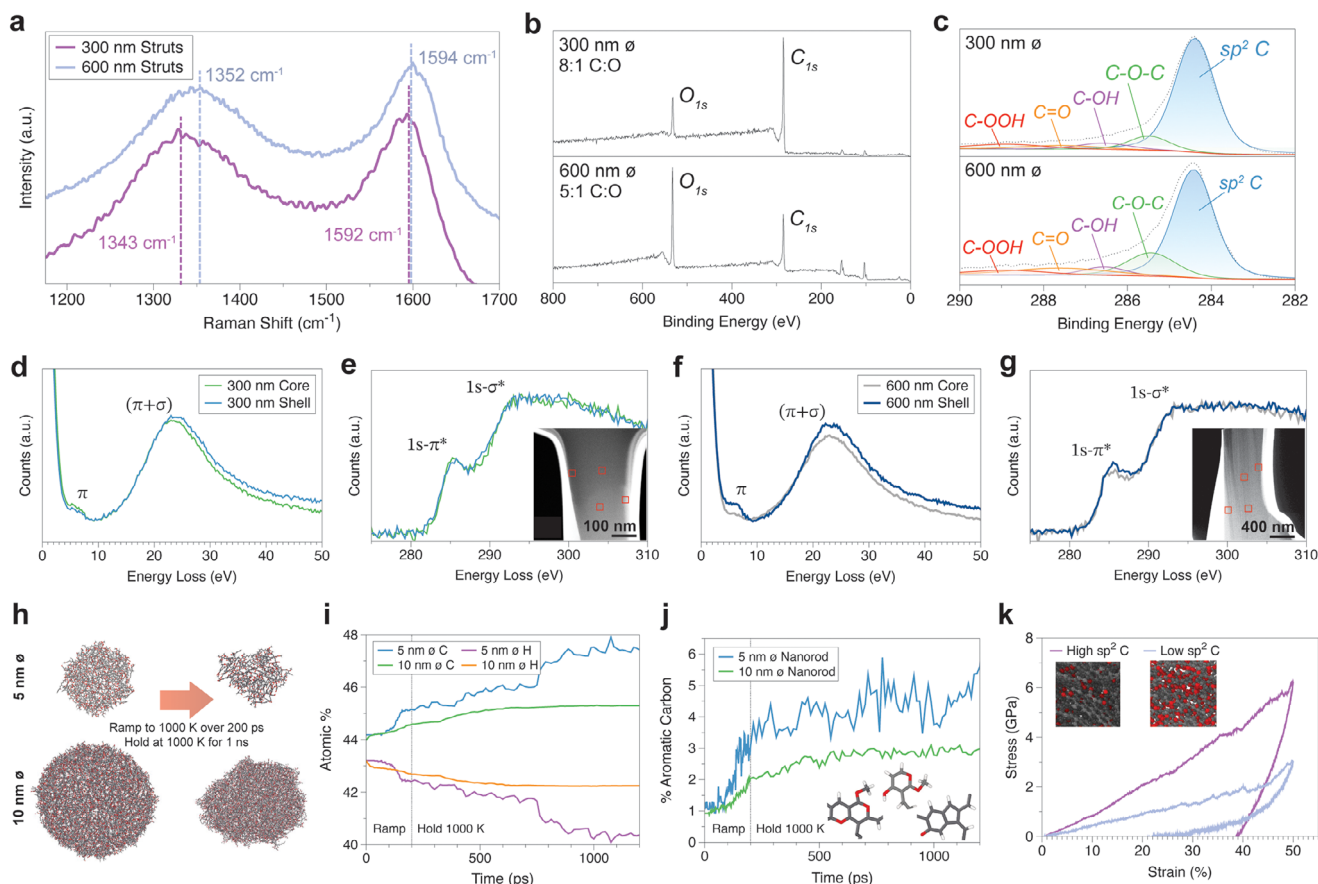
2410651 (6 of 11)

**ADVANCED
SCIENCE NEWS**

www.advancedsciencenews.com

**ADVANCED
MATERIALS**

www.advmat.de

Figure 4. Structural and atomic composition dependence of pyrolyzed carbon nanolattices with strut diameter. a) Raman spectra of A_{1g} and E_{2g} carbon phonon modes. b) XPS full spectra and c) C1s fitted spectra. d–g) EELS low-loss and core loss spectra for FIB-prepared cross sections of 300 and 600 nm struts, respectively. h) Molecular dynamics schematics of 5 and 10 nm nanorods subjected to pyrolysis. i) Atomic composition and j) Aromatic carbon composition of 5 and 10 nm nanorods during pyrolysis. k) MD uniaxial compression mechanics of simulated pyrolyzed carbon with replicated structural and atomic composition.

concentrations, an increase in the cross-sectional second moment of inertia, and greater load sharing across the lattice material which enables a greater elastic stiffness response.[31,32] Additionally, while the standard structure exhibits a progressive layer-by-layer localized failure beginning in the top row as is common in lightweight nanolattices,[33] the MBO structure shows only minimal damage at the boundary conditions at $\epsilon = 14\%$ prior to complete failure which occurs at $\epsilon = 17\%$. This is indicative of minimized stress concentrations which avoid localized premature failure at the nodes, thereby greatly increasing failure strength with failure occurring in the vertical strut members. These stiffness and failure mechanisms are in agreement with the FEA stress distributions and indicate notably different mechanical responses, despite equivalent densities, as enabled by the MBO beam element designs.

2.3. Nanoscale Pyrolyzed Carbon

In addition to MBO-iterated geometries, the ultrahigh specific strength of the carbon nanolattices is attributed to the constituent pyrolyzed carbon with nanoscale strut diameters. As per

Figure 2a,b, the lattices with 300 nm struts exhibit Young's moduli and strengths as much as 75% and 79% higher than lattices with 600 nm struts. Zhang et al., similarly identified compressive strengthening with strut diameter of pyrolyzed carbon proportional to $\sigma_y \propto D^{-0.36}$ and highlighted the role of internal porosity in microcrack nucleation and propagation.[11] Building upon this, we consider the atomic structure and transient pyrolysis process in enabling this mechanical enhancement. **Figure 4a** shows the Raman spectra for carbon nanolattices with 300 and 600 nm struts (larger lattices for characterization *cf.* Figure S27, Supporting Information). First, the 300 nm sample shows a Redshift of the A_{1g} band by 9 cm^{-1} as compared to the 600 nm struts indicative of longer bond lengths due to larger graphitic clusters.[34,35] Second, the I_D/I_G ratio increases from 2.19 to 2.83, which is proportional to average crystal sizes of $d = 1.9$ nm and $d = 2.2$ nm for the 600 and 300 nm struts, respectively (see Experimental Section and Equation 8).[34,36] Finally, the Full Width Half Max (FWHM) of the E_{2g} band is noted to increase from 80.9 to 87.3 cm^{-1} for the smaller struts which corresponds to the increasing presence of sp^2 content.[34] Thus, the 300 nm struts present greater sp^2-bonded aromatic carbon content as compared to the 600 nm struts.

**ADVANCED
SCIENCE NEWS**

www.advancedsciencenews.com

**ADVANCED
MATERIALS**

www.advmat.de

The atomic composition of the lattices also demonstrates a stark difference in X-ray photoelectron spectroscopy (XPS) C$1s$ to O$1s$ ratio, with an 8:1 C:O ratio for the 300 nm struts and a 5:1 ratio for the 600 nm struts (Figure 4b). The oxygen predominantly occurs in the form of C—O—C and C—OH impurities originating from the precursor pentaerythritol triacrylate polymer of the form $C_{14}H_{18}O_7$ (Figure 4c; Figure S28, Supporting Information).[37] This discrepancy in composition and structure with strut diameter occurs due to mass transport and impurity concentration during the transient pyrolysis process; the internal reaction and heat transfer rates are radially dependent on the dimensionless pyrolysis parameter in Equation (1)[38] and the desorptive mass flux during pyrolysis in Equation (2):[39]

$$P\gamma = \frac{\lambda}{(k\rho c_p r^2)} \tag{1}$$

$$S = \frac{\partial (\epsilon \rho)}{\partial t} + \frac{1}{r^2}\frac{\partial}{\partial r}\left(r^2 V\rho\right) \tag{2}$$

where S is volumetric mass desorption, λ, k, and c_p are thermal conductivity, apparent reaction rate constant, and specific heat capacity, and r, ρ, ϵ, t, and V are radius, density, porosity, time, and volume. The pyrolysis reaction rate is thus quadrupled and desorptive mass flux is doubled when the strut diameter is halved from 600 to 300 nm, which is in agreement with the reduced oxygen impurities noted for 300 nm struts. This also agrees with the experimental compilation by Cardenas–Benitez et al.,[40] which identifies greater mass and volume loss for thinner precursor polymers of both pentaerythritol triacrylate and SU-8 precursors.

In addition to the overall dependence on thickness, the pyrolysis rate and desorptive mass flux indicate an internal radial gradient. We perform electron energy loss spectroscopy (EELS) in localized 20 nm core and shell regions of focused-ion beam prepared strut cross-sections (Figure 4d–h, insets show scanning transmission electron microscope cross-sections). Using the two-window method for the integrated intensity of the $\pi*$ and $\sigma*$ states[41,42] (Equation (7) and Experimental Section), we determine the 300 nm strut to have 94% and 92% sp^2 bonding in the edge and center regions while the 600 nm strut has 95% sp^2 in the edge but only 82% in the center, indicating a distinct structural change with radius. It should be noted that while conventional nanowires have shell layers of 3–20 nm thickness,[43,44] the consistent bonding across the 300 nm thick struts suggests this high sp^2 bonded region spans at least across the 150 nm radius. This reveals why pyrolyzed carbon pillars show increasing strength with pillar diameter <10 μm[11] while typical nanowires only show this effect <200 nm[44] as the proportional volume of the larger high-strength shell becomes significant at larger sizes.

To understand the origin of this core-shell structure, we perform molecular dynamics (MD) simulations of the transient pyrolysis process using nanorods of up to 40 000 atoms (Figure 4h–j; Figures S29 and S30, Supporting Information). We create an elimination boundary condition whereby desorbed atoms are removed from the simulation and apply a pyrolysis ramp and hold temperature profile. We note a 2.1% difference in H atomic composition for the two nanorods after 1.2 ns as the 5 nm nanorod shows greater desorptive flux in agreement with Equation (2). This corresponds to a 2.2% increase in relative C

with a 3.3% increase in aromatic carbon formation (Figure 4i,j). Interestingly, the smaller nanorod shows greater mass loss but a higher density of 1020 kg m^{-3} compared to 830 kg m^{-3} for the larger nanorod. This suggests that the desorption of hydroxyl impurities is indeed a prerequisite for the formation of high-density aromatic carbon (Figure S29, Supporting Information). Further, the periphery and interior of the 10 nm nanorod show a difference in elemental and structural composition (Figure S31, Supporting Information) which confirms that the radial gradient structure indeed originates from pyrolysis. Modelling two volumes of material with mimetic composition to the interior and exterior regions of the pyrolytic carbon (Figure 4k; Figure S32, Supporting Information), we note an enhanced Young's modulus by 112% for the sp^2 rich and low O composition, highlighting the direct role of constituent pyrolytic carbon atomic structure on the mechanical response. Therefore, the mechanical enhancement of nanoscale-sized pyrolytic carbon is the result of size-dependent desorptive mass flux and the associated production of high-purity aromatic carbon during the transient pyrolysis process.

3. Discussion

This study demonstrates the synergistic effect of machine learning beam element optimization, high-purity pyrolyzed carbon, and nanoscale strut diameters to produce a nanolattice metamaterial with an ultrahigh specific strength of 2.03 MPa m^3 kg^{-1} at lightweight densities. We show that the MBO algorithm effectively explores and exploits the entire Pareto front to generate new beam elements that differ from its training data and offer 118% and 68% enhancement in strength and Young's modulus, respectively. Through scalable nano-additive manufacturing, this open-cell topology is applied toward the creation of an 18.75 million cell, 14.3 mm^3 material with macroscopic geometries. Finally, we show that the constituent pyrolytic carbon exhibits a gradient atomic structure of increased sp^2 aromatic carbon and lower oxygen impurities in the exterior, thereby enabling nanoscale strengthening. Collectively, this showcases the marked potential of machine learning in combination with nanoscale topologies to create exceptionall scalable metamaterials for contemporary engineering applications.

While this study aims to advance the capabilities of nanolattices by the introduction of machine learning-designed architectures, scalable manufacturing, and high-resolution characterization of the pyrolytic carbon atomic structure, there are several areas for further investigation. First, the MBO algorithm is executed using continuum mechanics based on FEA which does not capture size effects. MD simulations of a single 1.6 μm unit cell would require 10^{10} atoms and force fields capable of bond breakage which would lead to excessive computation times, however, a coupled FEA-MD approach may be fruitful.[45] Second, the scalable manufacturing of 18.75 million lattice cells demonstrates the applicability of these architectures but does not fully recapitulate the high mechanical performance of ideal nanolattices. Further optimization into pyrolysis of large-scale materials,[46] printing homogeneity and stitching,[28] and increasing throughput[30] are active fields of research that will be crucial toward the macroscopic adoption of nanolattices. Finally, in order to truly optimize the atomic structure of nanoscale pyrolytic carbon, further investigations into the magnitude of the sp^2 gradient and the role of

2410651 (8 of 11)

ADVANCED
SCIENCE NEWS
www.advancedsciencenews.com

ADVANCED
MATERIALS
www.advmat.de

different pyrolysis conditions on the desorptive mass flux and sp^2 aromatic carbon kinetics will enable accurate modeling and prediction of nanoscale size effects. Through the complete characterization and optimization of these multifaceted problems, we expect widespread impacts of nanoarchitected materials for many commercial applications.

4. Experimental Section

Multi-Objective Bayesian Optimization Training Data Generation: An automation macro for data generation was developed to produce the initial training data. This macro randomly generated control points, which formed the basis for creating the Bézier curve. Following this, a surface of revolution derived from the curve defined the shape of a beam segment and constituted the backbone of a unified lattice structure such as CFCC and CBCC. The homogenization method was adapted using finite element analysis, with each numerical analysis performed under two specified boundary conditions as follows:[47,48]

$$BC\ 1: \ \Delta l_x|_{x=l_x} = 0.1 l_x \text{ and } \Delta l_x|_{x=0} = \Delta l_y|_{y=0} = \Delta l_y|_{y=l_y} = \Delta l_z|_{z=0}$$
$$= \Delta l_z|_{z=l_z} = 0 \tag{3}$$

$$BC\ 2: \ \Delta l_x|_{z=l_x} = 0.05 l_z, \Delta l_z|_{x=l_z} = 0.05 l_x, \text{ and } \Delta l_z|_{x=0} = \Delta l_y|_{y=0}$$
$$= \Delta l_y|_{y=l_y} = \Delta l_z|_{z=l_z} = \Delta l_x|_{z=0} = 0 \tag{4}$$

From the analysis, the relative density ($\bar{\rho}$) and the volume-averaged value of the stress was calculated, from which the effective elastic constants $\overline{C_{11}}$, $\overline{C_{12}}$, and $\overline{C_{44}}$ for lattice structure were derived. Utilizing the effective elastic constants, relative to Young's modulus ($\bar{E}$) and relative shear modulus ($\bar{\mu}$) of a structure are calculated as follows:

$$\bar{E} = \frac{\overline{C_{11}}^3 + 2\overline{C_{12}}^3 - 3\overline{C_{11}}\,\overline{C_{12}}^2}{\overline{C_{11}}^2 - \overline{C_{12}}^2} \tag{5}$$

$$\bar{\mu} = \overline{C_{44}} \tag{6}$$

Multi-Objective Bayesian Optimization Algorithm: Inputs as the control points' coordinates (x_1, y_1, ..., x_4, y_4) for a Bézier curve were defined, with the objectives including relative Young's modulus, relative shear modulus, and specific volume (inverse relative density) ($\bar{E}$, $\bar{\mu}$, and $1/\bar{\rho}$). The optimization aimed to maximize the hypervolume encompassed by the values as objective ($\bar{E}$, $\bar{\mu}$, and $1/\bar{\rho}$). Multi-objective Bayesian Optimization (MBO) was employed, starting by fitting a Gaussian Process Regression (GPR) to the initial data, which yielded predictions on mean values and uncertainties. The acquisition function, specifically the Probability of Hypervolume Improvement (PHVI) and Expected Hypervolume Improvement (EHVI), was calculated using this model to guide the selection of subsequent sampling points based on these predictions. The chosen points were then evaluated using finite element analysis as material-agnostic linear-elastic calculations, with the outcomes integrated into the dataset to update the GPR model. This process was iteratively performed to explore the Pareto front, continuing until an additional 100 data points were included (see Figure S2, Supporting Information).

Two-Photon Polymerization: STL files of MBO topologies were patterned using Blender and exported as 5 × 5 × 5 STL files with fine resolution. The STL files were imported into DeScribe (Nanoscribe GmbH, Karlsruhe, Germany) and printed on a silicon wafer using Nanoscribe Photonic Professional GT2 system from IP-Dip2 Polymer (Nanoscribe GmbH,

Karlsruhe, Germany) at the Centre for Research and Applications in Fluidic Technologies (CRAFT) facility at the University of Toronto. The Nanoscribe PPGT2 system employed a 100 fs, 80 MHz pulsed laser, with a wavelength of 780 nm focused through a 63x objective. The beam had a Gaussian profile and was immersed in the IP-Dip2 resin during operation. Support bases with springs were printed using ΔY = 0.25 µm, ΔZ = 0.4 µm, P = 20 mW, and S = 10 mm s^{-1}. The nanolattices were printed using ΔY = 0.12 µm, Adaptive ΔZ = 0.3-0.05 µm, P = 17.5 mW, and S = 7.5 mm s^{-1}. All prints were performed with 30°/layer scan direction offset in order to ensure uniform mechanical properties and shrinkage in XY.

2PP Development: Sample development was based on procedures from the literature[1] and included: 1) Propylene glycol methyl ether acetate (PGMEA, also named SU8 Developer) for 15 min. 2) Fresh PGMEA for 2 h with gentle agitation by a 60 rpm stir stick. 3) Isopropyl alcohol (IPA) for 15 min. 4) Fresh IPA for 2h. 5) Removed from IPA and gently blow-dried the back of the Si wafer with N$_2$ gas. 6) 5 min blanket UV exposure.

Multi-Focus 2PP: The development of multi-photon multi-focus printing is described in detail in prior works.[29] A mode-locked laser source (790 nm, 3.7 W, 80 MHz, 140 fs; Coherent Chameleon Ultra II) was used in combination with a diffractive optical element and a multi-lens arrayed to generate a 7 × 7 = 49 focus array. A photoresist containing 0.5 wt.% BBK[30] was used in the monomer mixture IP-DIP NPI (Nanoscribe GmbH) with a 40x/NA1.4 objective lens (Carl Zeiss) to enable a lateral scan speed of $\upsilon = 1$ m s^{-1}. The hatching distance was set to 200 nm and the slicing distance to 300 nm. The lattice was printed using a sacrificial layer of 7 wt.% PVA in DI water which was spin-coated and subsequently removed by submerging in DI water.

Pyrolysis: Pyrolysis was carried out in a one-inch diameter ceramic furnace at atmospheric pressure under constant 400 mL min^{-1} with 70 kPa backpressure of 99.9% flowing N$_2$ gas throughout (Linde Canada plc., Mississauga, Canada). Prior to the pyrolysis process, N$_2$ gas was introduced into the chamber for 30 min in order to purge oxygen from the system. Pyrolysis conditions were: Ramp 7.5 °C min^{-1}–300 °C, Hold 1 h at 300 °C, Ramp 7.5 °C min^{-1}–900 °C, Hold 5 h at 900 °C, Cooled to Room Temperature naturally.

Mechanical Evaluation: Uniaxial compression of the nanolattices was performed using an iMicro Nanoindenter (KLA Corp.) with a 150 µm diameter diamond flat-punch tip. The compression was performed under constant displacement mode with a strain rate of 5 × 10^{-3} s^{-1}. Generated force-displacement curves were converted to stress–strain using individual lattice dimensions as determined by HRSEM imaging in order to account for any warping during pyrolysis. The Young's modulus was determined based on the 1–5% strain to account for the initial alignment regime typically noted in flat-punch compression.[1,12] The failure stress and strain of the lattices were determined as the maximum value before brittle failure.

In Situ Compression: In situ uniaxial compressive tests were conducted utilizing an Alemnis ASA nanoindenter housed within a Zeiss Gemini 450 scanning electron microscope (SEM), employing a 200 µm diameter diamond flat-punch tip. The compressive loading was applied at a controlled strain rate of 10^{-3} s^{-1} (quasi-static). The experimental setup included a standard load cell capable of measuring loads up to 2.5 N and a piezostack with a displacement range of 100 µm, enabling precise compression measurements. The compression protocol operated under displacement control, with a maximum displacement of 5 µm applied to the specimen during testing.

Finite Element Analysis Stress Visualizations: The finite element simulations were conducted using the ABAQUS software by Dassault Systèmes. The focus of the simulation was on a discretized unit cell, to which periodic boundary conditions were applied to replicate an infinite lattice. The fidelity of the periodic boundary condition was verified by comparing the response with a center cell within a 3 × 3 × 3 lattice structure which includes edge effects (see Figure S15, Supporting Information). For meshing, each unit cell utilized ten-node quadratic tetrahedral elements with better-represented curved boundaries and gradients in the field variables, known as C3D10 elements within the ABAQUS suite. The mesh density varied, with a range of 10–21 elements implemented through the thickness or diameter of the

struts. This variation was strategically chosen to enhance the simulation's accuracy and to capture the detailed stress distributions. The material properties inputted into the model were assumed to be linearly elastic. The Young's modulus was set at 2.1 GPa, and the Poisson's ratio was held constant at 0.15 adhering to the references in literature.[3,12] Stress distribution was particularly interesting in this project and measured in the principal stress across all the models.

Electron Microscopy: Field Emission Scanning electron microscopy (FESEM) images were taken using a SU7000 microscope (Hitachi Ltd., Tokyo, Japan) with an accelerating voltage of 10 kV and probe current of 30 nA.

Transmission electron microscopy (TEM), and Electron Energy Loss Spectroscopy (EELS) measurements were performed using a Hitachi HF-3300 TEM. The samples were prepared by Focused Ion Beam (FIB) lift-out and thinning of the strut cross-section as detailed in prior works.[49] TEM imaging was performed using an accelerating voltage of 100 kV. The accelerating voltage was selected based on comparable literature[11] and appropriate precautions were taken to minimize electron beam-induced artifacts.

sp^2 bonding was calculated from EELS using the two-window method of integrated intensities of the $\pi*$ and $\sigma*$ states in the core-loss peak using 284.7–285.3 eV for $\pi*$ states and 292–307 eV for $\sigma*$ states.[41,42] The bonding fraction was calculated in reference to pristine graphite which contains purely sp^2 bonds using Equation (7) where $\alpha = I_{\pi*}/I_{\sigma*}$:

$$f_{sp^2} = \frac{4\alpha_{PyC}/\alpha_G}{3 + \alpha_{PyC}/\alpha_G} \tag{7}$$

Raman Spectroscopy: High-frequency Raman spectra were collected using a Renishaw InVia microscope with an incident wavelength of 532 nm, 20× objective, and laser intensity of 2 mV from a diode-pumped solid-state laser. The spectral resolution was 1.9 cm^{-1} and the spatial resolution was 2 μm in diameter. Spectra were processed using Origin Pro to subtract background and a multi-peak fit was performed using Lorentzian fitting to calculate A_{1g} and E_{2g} peak location, intensity, and FWHM.[34] Average grain size was calculated based on the I_D/I_G ratio for a nanocrystalline/amorphous material with <20Å grain size as per Ferrari and Robertson[34,36] according to Equation (8):

$$d = \left(I_D/I_G/C'(\lambda)\right)^{0.5} \tag{8}$$

where C'(λ) is 0.6283 nm^{-2} for a 532 nm laser.

X-Ray Photoelectron Spectroscopy: X-ray Photoelectron Spectroscopy (XPS) characterization was performed at the Ontario Centre for the Characterization of Advanced Materials (OCCAM) using a Thermo Fisher Scientific K-Alpha system. Data collection and processing were performed with the Advantage package. Spectra were collected in a 50 μm box across the larger nanolattice (Figure S19, Supporting Information) with 0.1 eV resolution. Binding energy scales were shifted to center the adventitious carbon peak at 284.8 eV and peak fitting was done on a "Smart" background.

Molecular Dynamics Simulations: Molecular dynamics (MD) simulations were performed within the LAMMPS package[50] employing ReaxFF to describe interatomic interactions. A timestep of 0.5 fs was used, and the temperature and pressure were controlled with the Berendsen thermostat and barostat. The volumes, durations, and strain rates were acknowledged and used in MD simulation do not recapitulate the experimental conditions, however, the experimental trends that they mirror provide significant insight into the dynamics of these complex systems.

Pyrolysis Transient Dynamics MD Simulations: Pyrolysis simulations were done on nanorods of a representative precursor polymer. The polymer was modeled based on its known composition, with repetitive unit $C_{10}O_3H_{10}$ containing ester and hydroxyl groups. The polymer material was cross-linked and equilibrated as a bulk system at 300K and 1 atm. Following this, the system containing 9160 atoms was periodically expanded and carved into cylinders of 5 and 10 nm in diameter, with 4972 and 41028 atoms, respectively. These nanorods went through pyrolysis, during which

their axial direction was kept periodic at a constant length, with a 1:2 height/diameter ratio. Meanwhile, the other two directions contained a vacuum and allowed atoms to exit the system when they broke out of the material and moved away from it. The first step in the pyrolysis was a ramp from 300 to 1000K during 200 ps after which the system was kept at 1000K for 1000ps. Structural analysis during pyrolysis was performed with the aid of the ChemStruct Python package.

Compression Testing of Pyrolytic Carbon MD Simulations: For MD compression testing, the pyrolytic carbon material of the shell was modeled following a method established in the literature.[11] Graphene fragments were extracted from fullerene and rotated at random orientations, then placed in a closed-packed fashion in a simulation box of $10.5 \times 9.1 \times 8.4$ nm^3. Oxygen atoms were added as appended groups or substitutions, and hydrogen atoms were appended, yielding a final composition of 80% C, 13% O, and 7% H. The system was compressed at a 10^9 s^{-1} rate in every direction simultaneously until it reached a density of 1.4 g cm^{-3}. A melting-and-quenching process at NVT was then performed, increasing the temperature from 300 to 1200K in 50 ps, holding the temperature at 1200K for 300 ps, and decreasing it back to 300K in 50ps. This allowed the graphitic fragments to bond to one another. Finally, the final structure at 300K, and zero pressure for 200ps was equilibrated. All these steps were done within periodic boundary conditions, and the final system had dimensions of ca. $6.7 \times 5.4 \times 5.9$ nm^3. A similar method was used to model the amorphous carbon material of the core. The only differences were that the initial fullerene fragments were smaller and that the targeted composition was 60% C, 25% O, and 15% H, with the equilibrated system having $4.6 \times 4.0 \times 3.7$ nm^3. Finally, compression testing was performed on both bulk systems at a rate of 5×10^8 s^{-1} at 300K while allowing the two other dimensions of the cell to vary freely and maintaining periodic boundary conditions along every direction.

Supporting Information

Supporting Information is available from the Wiley Online Library or from the author.

Acknowledgements

Conflict of Interest

The authors declare no conflict of interest.

Data Availability Statement

The data that support the findings of this study are available in the supplementary material of this article.

Keywords

[1] C. Crook, J. Bauer, A. G. Izard, C. S. de Oliveira, J. M. de Souza e Silva, J. B. Berger, L. Valdevit, *Nat. Commun.* **2020**, *11*, 1579.

[2] R. Schwaiger, L. R. Meza, X. Li, *MRS Bull.* **2019**, *44*, 758.

[3] Y. Wang, X. Zhang, Z. Li, H. Gao, X. Li, *Proc. Natl. Acad. Sci. USA* **2022**, *119*, 2119536119.

[4] X. Zheng, H. Lee, T. H. Weisgraber, M. Shusteff, J. DeOtte, E. B. Duoss, J. D. Kuntz, M. M. Biener, Q. Ge, J. A. Jackson, S. O. Kucheyev, N. X. Fang, C. M. Spadaccini, *Science* **2014**, *344*, 1373.

[5] C. M. Portela, B. W. Edwards, D. Veysset, Y. Sun, K. A. Nelson, D. M. Kochmann, J. R. Greer, *Nat. Mater.* **2021**, *20*, 1491.

[6] M. Kagias, S. Lee, A. C. Friedman, T. Zheng, D. Veysset, A. Faraon, J. R. Greer, *Adv. Mater.* **2023**, *35*, 2209153.

[7] J. Bauer, L. R. Meza, T. A. Schaedler, R. Schwaiger, X. Zheng, L. Valdevit, *Adv. Mater.* **2017**, *29*, 1701850.

[8] X. Zhang, Y. Wang, B. Ding, X. D. Li, *Small* **2020**, *16*, 201902842.

[9] X. Feng, J. U. Surjadi, R. Fan, X. Li, W. Zhou, S. Zhao, Y. Lu, *Mater. Today* **2021**, *42*, 10.

[10] Y. M. Eggeler, K. C. Chan, Q. Sun, A. D. Lantada, D. Mager, R. Schwaiger, P. Gumbsch, R. Schröder, W. Wenzel, J. G. Korvink, M. Islam, *Adv. Funct. Mater.* **2023**, *34*, 2302068.

[11] X. Zhang, L. Zhong, A. Mateos, A. Kudo, A. Vyatskikh, H. Gao, J. R. Greer, X. Li, *Nat. Nanotechnol.* **2019**, *14*, 762.

[12] J. Bauer, A. Schroer, R. Schwaiger, O. Kraft, *Nat. Mater.* **2016**, *15*, 438.

[13] T. Frenzel, M. Kadic, M. Wegener, *Science* **2017**, *358*, 1072.

[14] D. Pasini, J. K. Guest, *MRS Bull.* **2019**, *44*, 766.

[15] C. M. Portela, J. R. Greer, D. M. Kochmann, *Extreme Mech Lett* **2018**, *22*, 138.

[16] L. R. Meza, S. Das, J. R. Greer, *Science* **2014**, *345*, 1322.

[17] S. Lee, Z. Zhang, G. X. Gu, *Mater Horiz.* **2022**, *9*, 952.

[18] S. Duan, L. Xi, W. Wen, D. Fang, *Compos. Struct.* **2020**, *238*, 111985.

[19] W. Deng, S. Kumar, A. Vallone, D. M. Kochmann, J. R. Greer, *Adv. Mater.* **2024**, *36*, 2308149.

[20] H. Jin, E. Zhang, H. D. Espinosa, *Appl. Mech. Rev.* **2023**, *75*, 061001.

[21] M. A. Bessa, P. Glowacki, M. Houlder, *Adv. Mater.* **2019**, *31*, 1904845.

[22] I. Kuszczak, F. I. Azam, M. A. Bessa, P. J. Tan, F. Bosi, *Extreme Mech Lett* **2023**, *64*, 102078.

[23] Z. Vangelatos, H. M. Sheikh, P. S. Marcus, C. P. Grigoropoulos, V. Z. Lopez, G. Flamourakis, M. Farsari, *Sci. Adv.* **2021**, *7*, 41.

[24] B. Peng, Y. Wei, Y. Qin, J. Dai, Y. Li, A. Liu, Y. Tian, L. Han, Y. Zheng, P. Wen, *Nat. Commun.* **2023**, *14*, 6630.

[25] N. A. Fleck, M. F. Ashby, V. S. Deshpande, *New Approaches to Structural Mechanics, Shells and Biological Structures*, Springer, Berlin, Germany **2002**.

[26] V. S. Deshpande, M. F. Ashby, N. A. Fleck, *Acta Mater.* **2001**, *49*, 1035.

[27] K. Refai, M. Montemurro, C. Brugger, N. Saintier, *Mechan. Adv. Mater. Struct.* **2020**, *27*, 1966.

[28] V. Hahn, P. Kiefer, T. Frenzel, J. Qu, E. Blasco, C. B. Kowollik, M. Wegener, *Adv. Funct. Mater.* **2020**, *30*, 1907795.

[29] P. Kiefer, V. Hahn, S. Kalt, Q. Sun, Y. M. Eggeler, M. Wegener, *Light: Adv. Manufac.* **2024**, *4*, 28.

[30] P. Kiefer, V. Hahn, M. Nardi, L. Yang, E. Blasco, C. Barner-Kowollik, M. Wegener, *Adv. Opt. Mater.* **2020**, *8*, 2000895.

[31] X. Ren, L. Xiao, Z. Hao, *Mater. Des.* **2019**, *174*, 107785.

[32] E. Ptochos, G. Labeas, *J. Sandwich Struct. Mater.* **2012**, *14*, 597.

[33] J. Bauer, S. Hengsbach, I. Tesari, R. Schwaiger, O. Kraft, *Proc Natl Acad Sci U S A* **2014**, *111*, 2453.

[34] A. C. Ferrari, J. Robertson, *Phys. Rev. B* **2000**, *61*, 14095.

[35] D. B. Schuepfer, F. Badaczewski, J. M. Guerra-Castro, D. M. Hofmann, C. Heiliger, B. Smarsly, P. J. Klar, *Carbon* **2020**, *161*, 359.

[36] P. Serles, M. Haché, J. Tam, A. Maguire, T. Li, G. Wang, K. Sebastian, J. Lou, C. Jia, P. M. Ajayan, J. Howe, Y. Zou, T. Filleter, *Carbon* **2023**, *201*, 161.

[37] Y. Liu, J. H. Campbell, O. Stein, L. Jiang, J. Hund, Y. Lu, *Nanomaterials* **2018**, *8*, 498.

[38] M. Brennan Pecha, J. I. M. Arbelaez, M. Garcia-Perez, F. Chejne, P. N. Ciesielski, *Green Chem.* **2019**, *21*, 2868.

[39] W. C. Park, A. Atreya, H. R. Baum, *Combust. Flame* **2010**, *157*, 481.

[40] B. Cardenas-Benitez, C. Eschenbaum, D. Mager, J. G. Korvink, M. J. Madou, U. Lemmer, I. D. Leon, S. O. Martinez-Chapa, *Microsyst. Nanoeng.* **2019**, *5*, 38.

[41] X. Zhang, R. Schneider, E. Müller, D. Gerthsen, *Carbon* **2016**, *102*, 198.

[42] F. Mangolini, Z. Li, M. A. Marcus, R. Schneider, M. Dienwiebel, *Carbon* **2021**, *173*, 557.

[43] G. F. Wang, X. Q. Feng, *J Phys D Appl Phys* **2009**, *42*, 155411.

[44] X. P. Zheng, Y. P. Cao, B. Li, X. Q. Feng, G. F. Wang, *Nanotechnology* **2010**, *21*, 205702.

[45] M. Yin, E. Zhang, Y. Yu, G. E. Karniadakis, *Comput. Methods Appl. Mech. Eng.* **2022**, *402*, 115027.

[46] K. Baglo, M. Sauermoser, M. Lid, T. Paschke, A. B. Afif, M. Lunzer, A. Flaten, M. Steinert, R. Bock, J. Torgersen, *Adv. Mater. Technol.* **2023**, *8*, 2300092.

[47] P. Tan, L. Tong, G. P. Steven, *Compos. A Appl. Sci. Manuf.* **2000**, *31*, 273.

[48] S. Xu, J. Shen, S. Zhou, X. Huang, Y. M. Xie, *Mater. Des.* **2016**, *93*, 443.

[49] P. Serles, H. Sun, G. Colas, J. Tam, E. Nicholson, G. Wang, J. Howe, A. Saulot, C. V. Singh, T. Filleter, *Adv. Mater. Interfaces* **2020**, *7*, 19018701.

[50] S. Plimpton, *J. Comput. Phys.* **1995**, *117*, 1.